Understanding the reverse time migration backscattering: Noise or signal?

Esteban Díaz and Paul Sava
Center for Wave Phenomena, Colorado School of Mines, Golden CO 80401

ABSTRACT
Reverse time migration (RTM) backscattered events are produced by the cross-correlation between waves reflected from sharp interfaces (e.g. the top of salt bodies). These events, along with head waves and diving waves, produce the so-called RTM artifacts, which are visible as low wavenumber energy on migrated images. Commonly, these events are seen as a drawback for the RTM method because they obstruct the image of the geologic structure, which is the real objective for the process. Many strategies have been developed to filter out the artifacts from the conventional image. However, these events contain information that can be used to analyze kinematic synchronization between source and receiver wavefields reconstructed in the subsurface. Numeric and theoretical analysis indicate the sensitivity of the backscattered energy to velocity accuracy: an accurate velocity model maximizes the backscattered artifacts. The analysis of RTM extended images can be used as a quality control tool and as input to velocity analysis to constrain salt models and sediment velocity.

Key words: RTM backscattering, wavefield decomposition, migration velocity analysis

1 INTRODUCTION

Reverse time migration (RTM) is not a new imaging technique (Baysal et al., 1983; Whitmore, 1983; McMechan, 1983). However, it was not until the late 1990s, and mainly the 2000s that computational advances allowed the geophysical community to use this technology for exploratory 3D surveys. In general, and especially in complex geological settings, RTM produces better images than other methods. Imaging methods such as Kirchhoff migration and one-way equation migration are based on approximate solutions to the wave equation. Kirchhoff migration, a high frequency asymptotic solution to the wave equation, becomes unstable for complex velocity models. This technique also fails to easy handle multipathing and typically creates the images based on a single travel-time arrival (e.g. most energetic or first arrival). Other methods based on approximations to the wave equation, such as phase shift migration (Gazdag, 1978), rely on a v(z) earth model and further approximations are needed to account for lateral variations (Gazdag and Sguazzero, 1984). In addition to earth model considerations, one-way wave equation migration propagate the wavefields in either the upward or the downward direction; this approximation becomes inexact when the waves propagate horizontally. Therefore, this technique fails to properly handle overturning waves and reflections from steep-dip structures. RTM's propagation engine, a two-way wave equation, makes this imaging method robust and accurate because it honors the kinematics of the wave phenomena by allowing waves to propagate in all directions regardless of the velocity model or the direction of propagation. This method also takes into account, in a natural way, multipathing and reflections from steep dips.

A striking characteristic of RTM is the presence of low wavenumber events in the image that are uncorrelated with the geology. The two-way wave equation simulates scattered waves in all directions. Therefore, the imaging condition produces new events not observed in other imaging methods that correspond to the cross-correlation between diving waves, head waves and backscattered waves. The cross-correlation between the backscattered waves is more visible in presence of sharp boundaries (e.g. the top of salt) which produces strong events that mask the image of the earth reflectivity above the salt. The backscattered events are considered as noise and are normally filtered in order to get the image of earth reflectivity.

The seismic industry has dedicated effort and time developing algorithms and strategies to filter out the backscattered energy from the image. We can classify the filtering approaches in two general families: pre-imaging condition and post-imaging condition.

The pre-imaging condition family modify the wavefields (either by modeling or wavefield decomposition) in such a way that the backscattered events do not form during the imaging

process. One strategy in the pre-imaging condition category is wavefield decomposition (Liu et al., 2011; Fei et al., 2010). In this method, the source and receiver wavefield are decomposed in upgoing and downgoing directions. In the imaging step, we cross-correlate only the wavefields that propagate in opposite directions producing an image which corresponds to the geology. The cross-correlation between wavefields traveling in parallel directions is discarded because produce events that obstructs the geology. Other pre-imaging condition approaches are performed by modifying the wave equation to attenuate the reflections coming from sharp interfaces (Fletcher et al., 2005). A similar method applicable to post-stack migration uses impedance matching at sharp interfaces (Baysal et al., 1984).

In the post-imaging family, the artifacts are attenuated by filtering. These filtering approaches are considerably cheaper because they operate in the image space and not on the wavefields. A straightforward approach is to apply a Laplacian operator to the image (Youn and Zhou, 2001); this operator acts as a high pass filter and is effective because the backscattered events have a strong low wavenumber component. A second strategy is a signal/noise separation by least squares filtering. In this case the signal is defined as the reflectivity and the noise is the backscattered energy (Guitton et al., 2007). Finally, extended imaging conditions (Rickett and Sava, 2002; Sava and Fomel, 2006; Sava and Vasconcelos, 2011) provide information about the wavefield similarity for different space and/or time lags and can also be used to discriminate the backscattered energy. Kaelin and Carvajal (2011) take advantage of the way backscattered events appear in time-lag gathers. The backscattered events map toward zero time-lag when a correct velocity model is used for imaging, whereas the primary reflections map within a limited slope range constrained by the velocity model. This difference in slope allows us to design 2D filters that preserve events within the primaries reflections range and attenuate the backscattered energy.

In this report we analyze the information carried by the backscattered energy in the extended images. We show that the backscattered waves provide important information about the synchronization between the reconstructed wavefields in the subsurface, i.e. an image obtained with a correct velocity model shows maximum backscattered energy. The presence of backscattered energy in the image not only depends on the interpretation of the sharp interface but also on the velocity above it. We analyze the mapping patterns of the backscattered events in the extended images using wavefield decomposition approaches and conclude that backscattered energy is sensitive to the velocity model accuracy and therefore should be included as a source of information to migration velocity analysis (MVA). Counter to common practice, we assert that backscattering artifacts should be enhanced during RTM to constrain the velocity models, and they should only be removed in the last stage of imaging.

2 WAVE EQUATION IMAGING CONDITIONS

2.1 Conventional imaging condition

The conventional imaging condition (Claerbout, 1985) is a zero time lag cross-correlation between the source wavefield and the receiver wavefields:

$$R(\mathbf{x}) = \sum_{shots} \sum_{t} W_s(\mathbf{x}, t) W_r(\mathbf{x}, t), \tag{1}$$

which honors the single scattering or Born assumption. Under this assumption the transmitted source wavefield generates secondary waves as it interacts with the medium discontinuities. These secondary waves propagate in space and are recorded at the surface. This assumption means that both the source and receiver wavefields carry only transmitted energy through interfaces between layers with different elastic properties.

A wavefield extrapolated with RTM could show, depending on the complexity of the geology, waves traveling in both upward and downward directions, such as diving waves, head waves and backscattered waves. The interaction between these waves contained in the source and receiver wavefields generates new events in the image which are commonly referred to as artifacts because they do not follow the geology (i.e. earth reflectivity), which is the objective of the imaging process. The correlation between forward and backscattered waves is particularly strong when sharp boundaries are present in the velocity model (e.g. salt bodies).

If a sharp boundary is present in the model, we can decompose the source wavefield into transmitted and reflected energy that originates at the sharp boundary:

$$W_s(\mathbf{x}, t) = W_s^r(\mathbf{x}, t) + W_s^t(\mathbf{x}, t), \tag{2}$$

where the superscripts t and r stand for transmitted and reflected energy, respectively.

The same idea can be applied to the receiver wavefield:

$$W_r(\mathbf{x}, t) = W_r^r(\mathbf{x}, t) + W_r^t(\mathbf{x}, t). \tag{3}$$

By taking advantage of the linearity of equation 1, we can split the conventional imaging condition as follows:

$$\begin{aligned} R(\mathbf{x}) = {} & R^{tt}(\mathbf{x}) + R^{rr}(\mathbf{x}) \\ & + R^{tr}(\mathbf{x}) + R^{rt}(\mathbf{x}). \end{aligned} \tag{4}$$

Here, the first superscript is associated with the source wavefield and the second is associated to the receiver wavefield. For example, $R^{tr}(\mathbf{x})$ is an image constructed with the transmitted source wavefield and the reflected receiver wavefield.

By analyzing the individual contributions to the image, we can better understand how the backscattered events are constructed in the image. This analysis is similar to the one of Fei et al. (2010) and Liu et al. (2011) whose objective is to filter out the non-geological portions of the image. Here, we approach the problem in a broader sense by attempting to un-

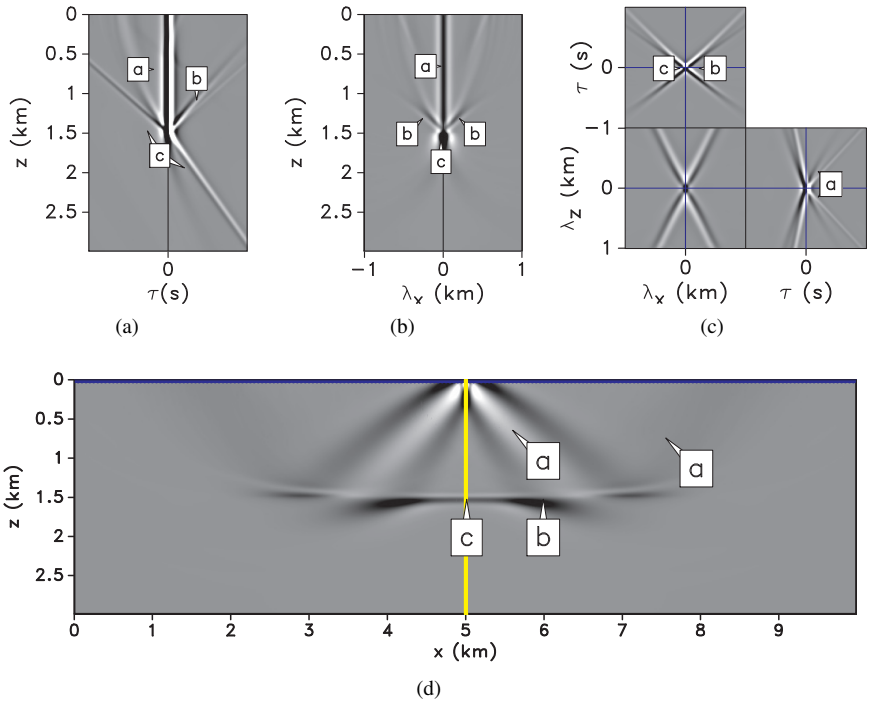


Figure 1. Synthetic model example: (a) time-lag gather at x=5km, (b) space-lag gather at x=5km, (c) common image point at x=5km, z=1.5km and (d) migrated image of one shot (in x=5km,z=0km) with receivers in the surface

derstand the physical meaning of the backscattered energy and its uses for velocity model building.

2.1.1 Backscattered events in the conventional image

In order to gain an understanding of the RTM backscattered events, we use a simple model with two-layers and strong velocity contrast. Figure 1(d) shows the image obtained with the conventional imaging condition for one shot at $x = 5km$. This image has strong backscattered energy, indicated with letter "a", above the reflector located at $z = 1.5km$.

To better understand the origin of the backscattered artifacts, we illustrate the wavefields used for imaging our simple model. Figures 2(a), 2(e) and 2(i) show three different snapshots of the source wavefield. Likewise, Figures 2(b), 2(f) and 2(j) show the same snapshots for the receiver wavefield. Figures 2(c), 2(g) and 2(k) show the product between source and receiver wavefields for the same time snapshots. Finally, Figures 2(d), 2(h) and 2(l) show the accumulated image as a function of time (integration over time of the product between wavefields).

Figure 2(d) show the interaction between the transmitted source wavefield W_s^t, shown in Figure 2(a), and the reflected receiver wavefield W_r^r shown in Figure 2(b). In this case, the reflected receiver wavefield travels in perfect synchronization with the transmitted source wavefield, therefore their product, shown in Figure 2(c), stacks coherently in the imaging process generating the $R^{tr}(\mathbf{x})$ contribution to the image $R(\mathbf{x})$. In the $R^{tr}(\mathbf{x})$ image, the reflected receiver wavefield behaves as the transmitted source wavefield, which is the reason why the backscattered energy is imaged toward the source location. In the partial image at $t = 0.275s$, shown in Figure 2(h), we see how we start building the reflector image. The reflected source wavefield, shown in Figure 2(e), generates new backscattered events corresponding to the $R^{rt}(\mathbf{x})$ image. In the snapshot at $t = 0.5s$, the reflector is completely imaged and for remaining time we only add backscattered energy corresponding to the $R^{rt}(\mathbf{x})$ image. In this case the reflected source wavefield behaves as the receiver wavefield and its energy maps toward the receivers. We can see that after the imaging process is finished, Figure 1(d), that the backscattered energy is maximum near the critical angle range (where the reflected source and receiver wavefields have maximum energy).

Using wavefield decomposition allow us to isolate the individual contributions of equation 4. Figure 3(a) shows the cross-correlation between transmitted wavefields, producing an image due to the earth reflectivity. Figures 3(b) and 3(c) show the images $R^{tr}(\mathbf{x})$ and $R^{rt}(\mathbf{x})$ corresponding to the backscattered energy, which maps toward the source and the receivers, respectively. The image corresponding to the $R^{rr}(\mathbf{x})$, shown in Figure 3(d), contains additional contribution to the reflectivity of the earth due to the cross-correlation between reflected wavefields. Fei et al. (2010) take advantage of this analysis to define an image free from backscattered energy as $R(\mathbf{x}) = R^{tt}(\mathbf{x}) + R^{rr}(\mathbf{x})$. Here, we want to better understand the meaning and uses of the other two partial images $R^{tr}(\mathbf{x})$ and $R^{rt}(\mathbf{x})$.

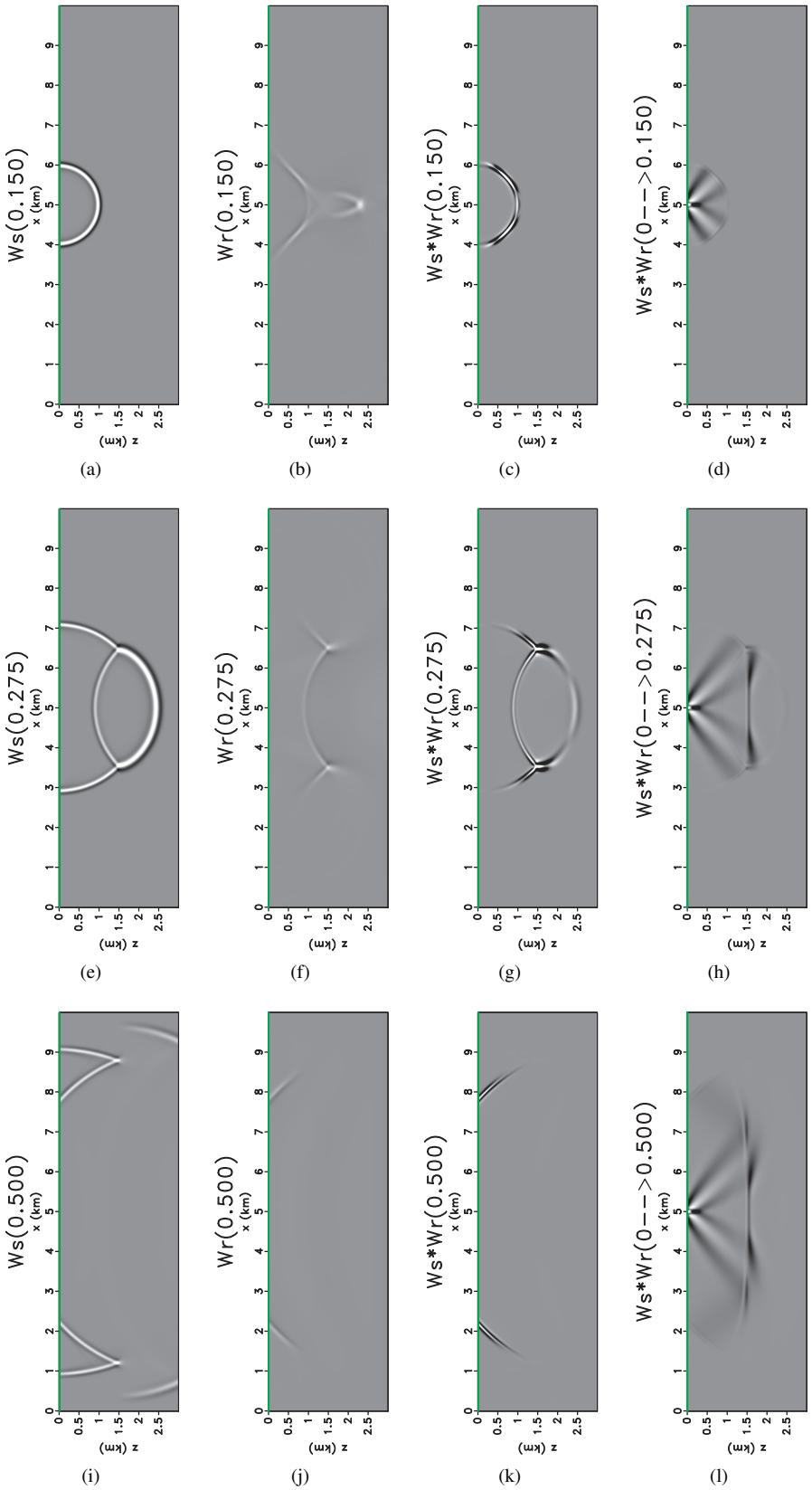


Figure 2. Pictorial explanation of RTM imaging: rows 1, 2 and 3 correspond to three different snapshots at times $t_1 = 0.150s$, $t_2 = 0.275s$ and $t_3 = 0.500s$. Columns 1 to 4 correspond to the source wavefield, the receiver wavefield, the multiplication of the source and receiver wavefields, and the accumulated image over time, respectively.

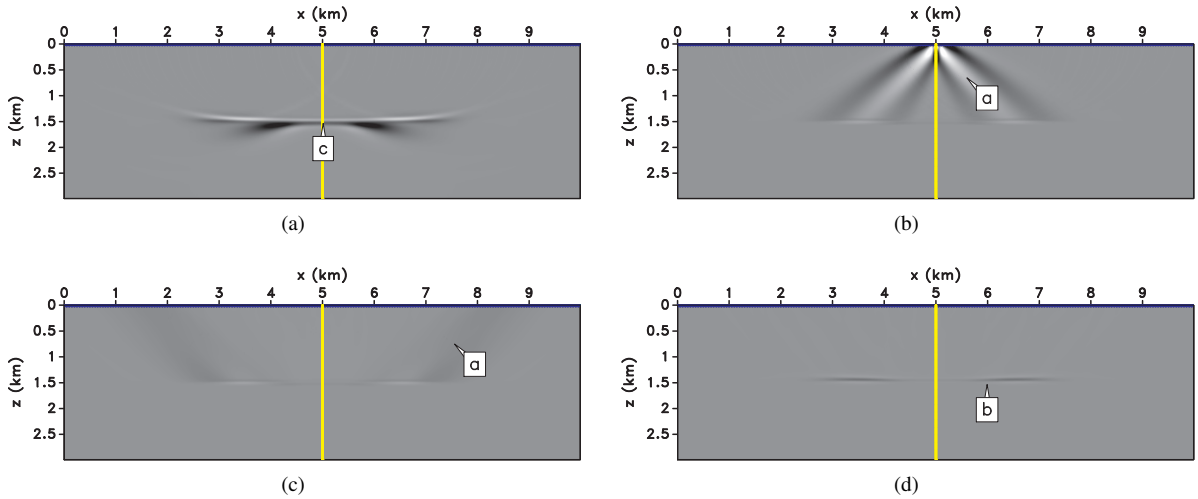


Figure 3. Illustration of the linearity of the conventional imaging condition. We can split the conventional image, Figure 1(d), in four separate images, $R^{tt}(\mathbf{x})$ (a), $R^{tr}(\mathbf{x})$ (b), $R^{tr}(\mathbf{x})$ (c), and $R^{rr}(\mathbf{x})$ (d), corresponding to the correlation of the transmitted and/or reflected components of the source and receiver wavefields

2.2 Extended imaging condition

The extended imaging condition (Rickett and Sava, 2002; Sava and Fomel, 2006; Sava and Vasconcelos, 2011) is similar to the conventional imaging condition except the cross-correlation lags between source and receiver wavefield are preserved in the output:

$$R(\mathbf{x},\boldsymbol{\lambda},\tau) = \sum_{shots}\sum_{t} W_s(\mathbf{x}-\boldsymbol{\lambda},t-\tau)W_r(\mathbf{x}+\boldsymbol{\lambda},t+\tau). \tag{5}$$

Here $\boldsymbol{\lambda}$ and τ represent the space-lags and time-lags, respectively, of the cross-correlation. The conventional image is a special case of the extended image $R(\mathbf{x}) = R(\mathbf{x},\mathbf{0},0)$.

By using extended images, we can measure the accuracy of the velocity model by analyzing the moveout of the events (Yang and Sava, 2010), and we can perform transformations from the extended to the angle domain (Sava and Fomel, 2003, 2006; Sava and Vlad, 2011). The extended images provide a measurement of the similarity between the source and receiver wavefields along space and time, so we can exploit these images to analyze and better understand the RTM backscattered events.

In equation 5 we observe an increase in the dimensionality of the image, from 3 to 7 dimensions, if we decide to extend the image in all directions. It is common to perform the analysis of extended images at limited locations in order to make this methodology feasible for large datasets. For cost considerations we often use an extension for common image gathers (CIG), for instance the time-lag axis (τ) or the space-lag axis (λ_x). We can also consider common image point gathers (CIP), where we fix an observation point $\mathbf{c} = (x,y,z)$ and analyze the image as a function of extensions $\boldsymbol{\lambda},\tau$.

Figures 1(a) to 1(c) show a time-lag gather, a space-lag gather, and a common image point, respectively, which represent subsets at fixed surface positions (for CIGs) or fixed space positions (for CIPs). Despite the fact that our model has only one reflector, we can identify several events in the conventional and extended images. Letter "a" indicates backscattered events, letter "b" indicates the events produced by the cross-correlation of reflected wavefields, and letter "c" indicates the cross-correlation between transmitted wavefields.

In the presence of sharp velocity interfaces we can use the concept of equation 4, and construct four partial extended images:

$$\begin{aligned} R(\mathbf{x},\boldsymbol{\lambda},\tau) = {} & R^{tt}(\mathbf{x},\boldsymbol{\lambda},\tau) + R^{rr}(\mathbf{x},\boldsymbol{\lambda},\tau) \\ & + R^{tr}(\mathbf{x},\boldsymbol{\lambda},\tau) + R^{rt}(\mathbf{x},\boldsymbol{\lambda},\tau). \end{aligned} \tag{6}$$

2.2.1 Time-lag common image gathers

Using equation 6, we analyze the individual contributions for the time-lag gather shown in Figure 1(a). Figure 4(a) shows the image $R^{tt}(z,\tau)$ with a change in the slope of the events due to the abrupt velocity variation of the model. Above the reflector depth, the slope is controlled by the velocity of layer 1, whereas below the interface the slope is controlled by the velocity of layer 2. Figures 4(c) and 4(b) show the backscattered event contributions $R^{tr}(z,\tau)$ and $R^{rt}(z,\tau)$, respectively, which indicate that the backscattered event maps towards τ=0 in the extended image. This means that we only get a contribution when we do not dislocate the wavefields by shifting them in time, thus reinforcing the idea of wavefield synchronization. Figure 4(d) shows the $R^{rr}(z,\tau)$ image; in this case the source wavefield is going in the upward direction and the receiver wavefield is going in the downward direction, which is as if we change the order of cross-correlation in equation 5. This is why these events map in the time-lag gathers

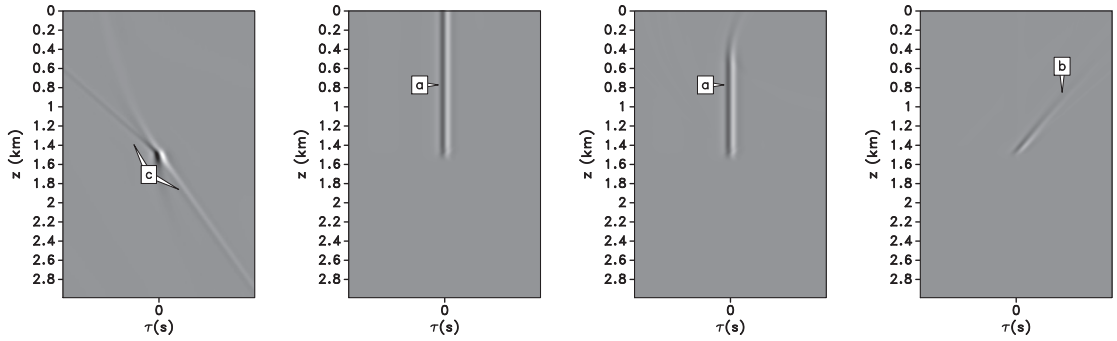


Figure 4. Illustration of the linearity of the time-lag extended imaging condition. We can split a time-lag gather, Figure 1(a), in four separate images, $R^{tt}(z,\tau)$ (a), $R^{rt}(z,\tau)$ (b), $R^{tr}(z,\tau)$ (c) and $R^{rr}(z,\tau)$ (d), corresponding to the correlation of the transmitted and/or reflected components of the source and receiver wavefields

with a slope opposite to the primary above the interface. Because the reflected waves only travel in the upper layer, we observe this image above the reflector. In the $R^{rr}(z,\tau)$ image we see two events that map with similar slope, one has the exact opposite slope as the one shown by the primary reflection, the other has a slightly higher slope (therefore indicating faster velocity) and corresponds to the interaction between head-waves produced by the velocity discontinuity and the reflected wavefields. In the time-lag gathers the slope of the primaries is very different from the backscattered events slope. Kaelin and Carvajal (2011) use the slope difference to filter the backscattered events in this domain and to extract the conventional image from the filtered extended image $R(\mathbf{x})$=$R(\mathbf{x},\tau$=0).

2.2.2 Space-lag common image gathers

Figure 1(b) shows a space-lag gather for the various combinations of the source and receiver wavefield components. We note that with the correct velocity model, both primaries and backscattered events map to $\lambda_x = 0$ since the velocity used for imaging is correct. Figure 5(a) shows the $R^{tt}(z,\lambda_x)$ image with the energy correctly focused at $\lambda_x = 0$. Figures 5(b) and 5(c) show the backscattered events $R^{rt}(z,\lambda_x)$ and $R^{tr}(z,\lambda_x)$ in the space-lag gathers, which also map toward $\lambda_x = 0$. Figure 5(d) shows the image coming from the reflected wavefields $R^{rr}(z,\lambda_x)$; in this case the events are visible only above the reflector because the waves travel only in the first layer.

2.2.3 Common-image point gathers

The events involving backscattered energy are also visible in CIP gathers. Figure 1(c) shows a CIP extracted at $\mathbf{c}$=$(5,1.5)km$. Figure 6(a) shows the CIP for the transmitted wavefields $R^{tt}(\mathbf{x},\boldsymbol{\lambda},\tau)$. The energy focuses at zero lag for the $\tau-\lambda_x$ panel. The $\lambda_z-\tau$ shows a kink produced by the abrupt change in velocity for the primaries, which are mapped at negative τ. Figure 6(c) shows the $R^{tr}(\mathbf{x},\boldsymbol{\lambda},\tau)$ image, and we can see a change in the $\lambda_z-\tau$ plane, where the backscattered energy is mapped to positive lags. Figure 6(b) shows the complementary backscattered energy that is mapped to negative λ_z and positive τ lags. The CIP from the reflected wavefields, Figure 6(d), shows weak energy concentrated at zero lags.

3 SENSITIVITY TO VELOCITY ERRORS

In this section, we test the dependency of the backscattered energy on velocity errors using extended images. In the previous sections we have explained the concept of wavefield synchronization for correct velocity, which implies that for correct velocity the backscattered energy maps toward zero lags. Here, we analyze the behavior of backscattered events in the presence of velocity errors. We test the sensitivity of the backscattered events with the same synthetic data discussed previously. In this case, we construct the images with different models characterized by a constant error varying from -12% to +12% in layer 1. We keep the interface consistent with the velocity used for imaging, i.e. we assume that the interface producing backscattered energy is placed in the model according to the velocity in layer 1. Figures 7(a) to 7(i) show time-lag gathers as a function of the velocity error. The backscattered energy is still mapped vertically, but away from τ=0. The backscattered events in the time-lag gathers show a kinematic error, i.e. these events move from positive τ for negative errors to negative τ values for positive errors. Figures 8(b) to 8(i) show a similar display for space-lag gathers. In this case, both, backscattered and primary energy map away from λ_x=0 when we introduce an error in the model. In space-lag gathers, the backscattered energy maps symmetrically away from zero lag with incorrect velocities. Finally, Figures 9(b) to 9(i) show the sensitivity of CIPs to velocity errors. For incorrect velocity, the events move away from zero-lags. In the CIPs, even when constructed with incorrect velocity, the primary reflections go trough zero-lag, and the events in the $\tau-\lambda_x$ plane show moveout (i.e. the energy not mapped symmetrically respect zero lag). The velocity errors split the backscattered energy in the $\lambda_z-\tau$ plane, some

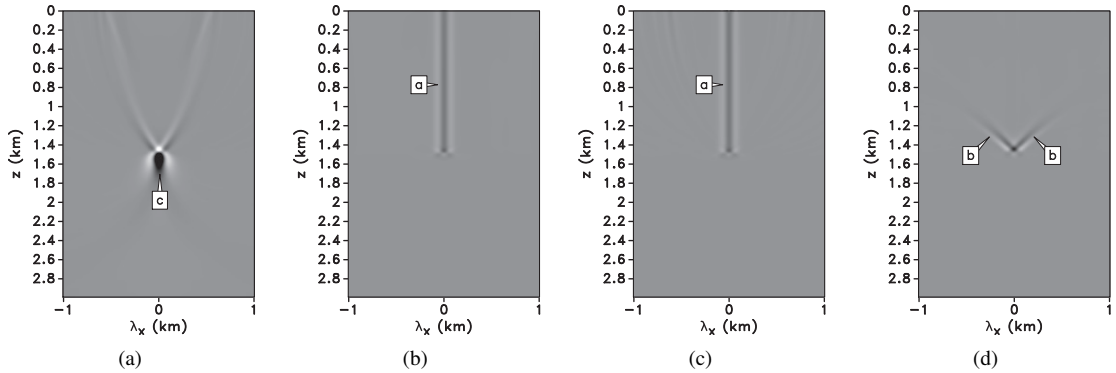


Figure 5. Illustration of the linearity of the space-lag extended imaging condition. We can divide Figure 8(e) in four images, $R^{tt}(z,\lambda_x)$ (a), $R^{rt}(z,\lambda_x)$ (b), $R^{tr}(z,\lambda_x)$ (c) and $R^{rr}(z,\lambda_x)$ (d), corresponding to the correlation of the transmitted and/or reflected components of the source and receiver wavefields

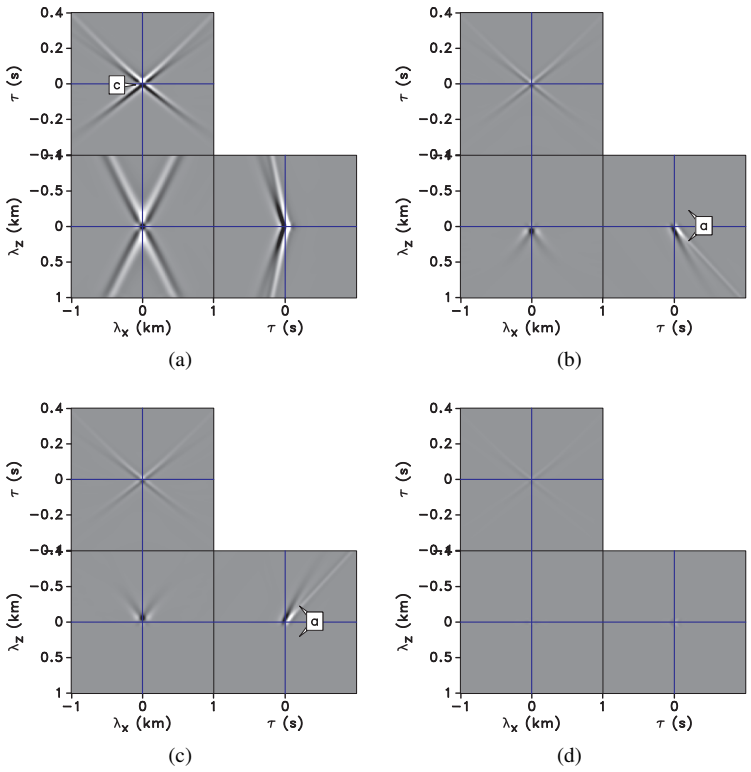


Figure 6. Illustration of the linearity of the extended imaging condition for a common image point. We can decompose a CIP, Figure 9(e), in four images $R^{tt}(\boldsymbol{\lambda},\tau)$ (a), $R^{rt}(\boldsymbol{\lambda},\tau)$ (b), $R^{tr}(\boldsymbol{\lambda},\tau)$ (c), $R^{rr}(\boldsymbol{\lambda},\tau)$ (d) corresponding to the correlation between transmitted and/or reflected components of the source and receiver wavefields

of the energy goes trough zero space-lag while other part of the energy does not.

We could use the information contained in the extended images to design objective functions (OF) that exploit the presence of backscattered events. Minimizing such OF, e.g. by wavefield tomography, optimizes the sharp interface positioning (e.g. the top of salt) and the sediments velocity above it. A straightforward approach based on differential semblance optimization (Shen et al., 2003) can be adapted to use the backscattered energy seen away from zero lags by defining the objective functions for time-lag gathers

$$J_\tau = \frac{1}{2}\|P(\tau)\left[R^{tr}(\mathbf{x},\tau)+R^{rt}(\mathbf{x},\tau)\right]\|_2^2, \qquad (7)$$

and for the space-lag gathers,

$$J_{\lambda_x} = \frac{1}{2}\|P(\lambda_x)\left[R^{tr}(\mathbf{x},\lambda_x)+R^{rt}(\mathbf{x},\lambda_x)\right]\|_2^2. \qquad (8)$$

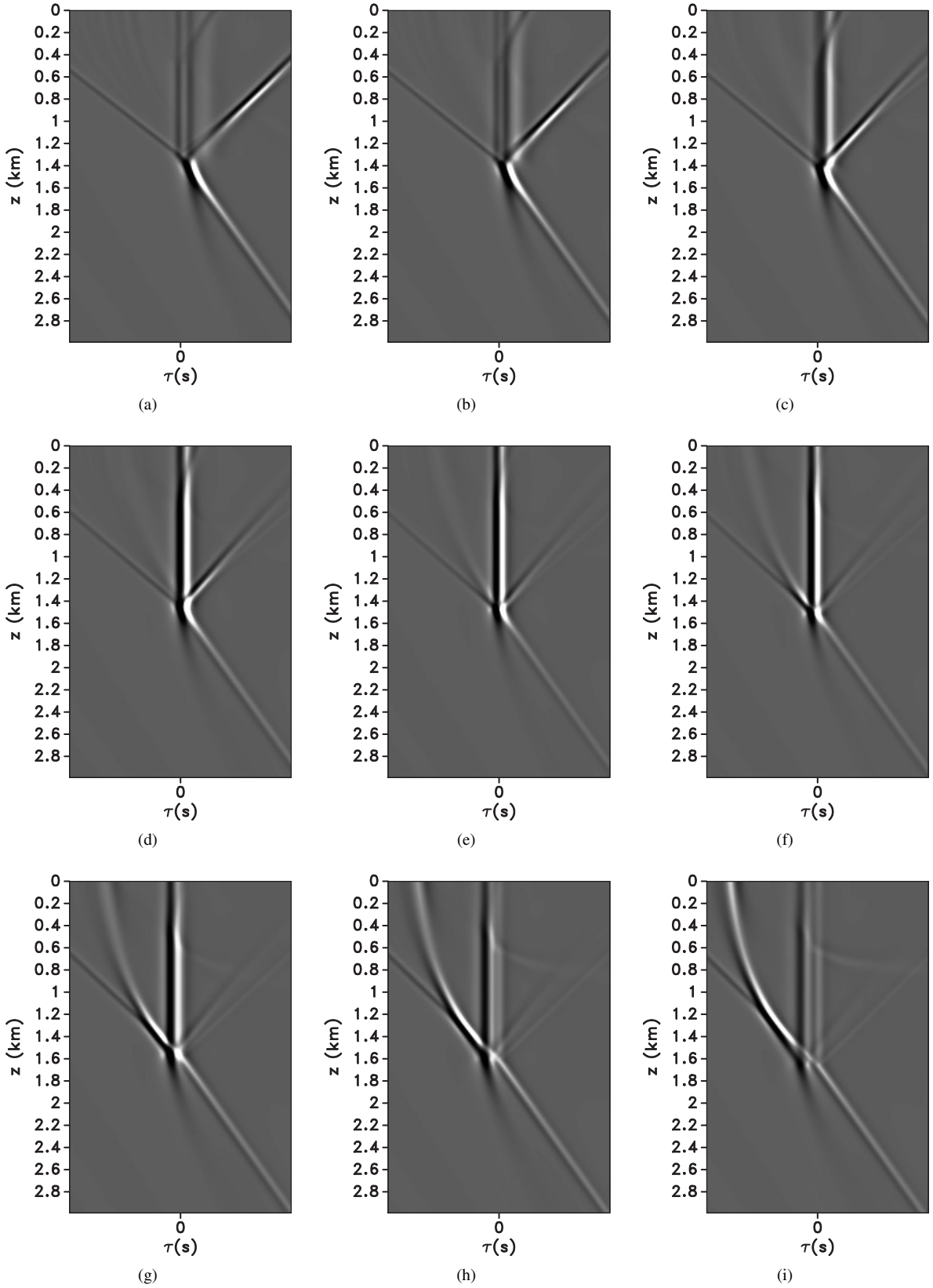


Figure 7. Model error sensitivity with time-lag gathers: (a) -12%, (b) -9%, (c) -6%, (d) -3%, (e) 0%, (f) +3%, (g) +6%, (h) +9% and (i) +12% velocity perturbation in the top layer. The maximum energy of the backscattered events occur with correct velocity shown in panel (e).

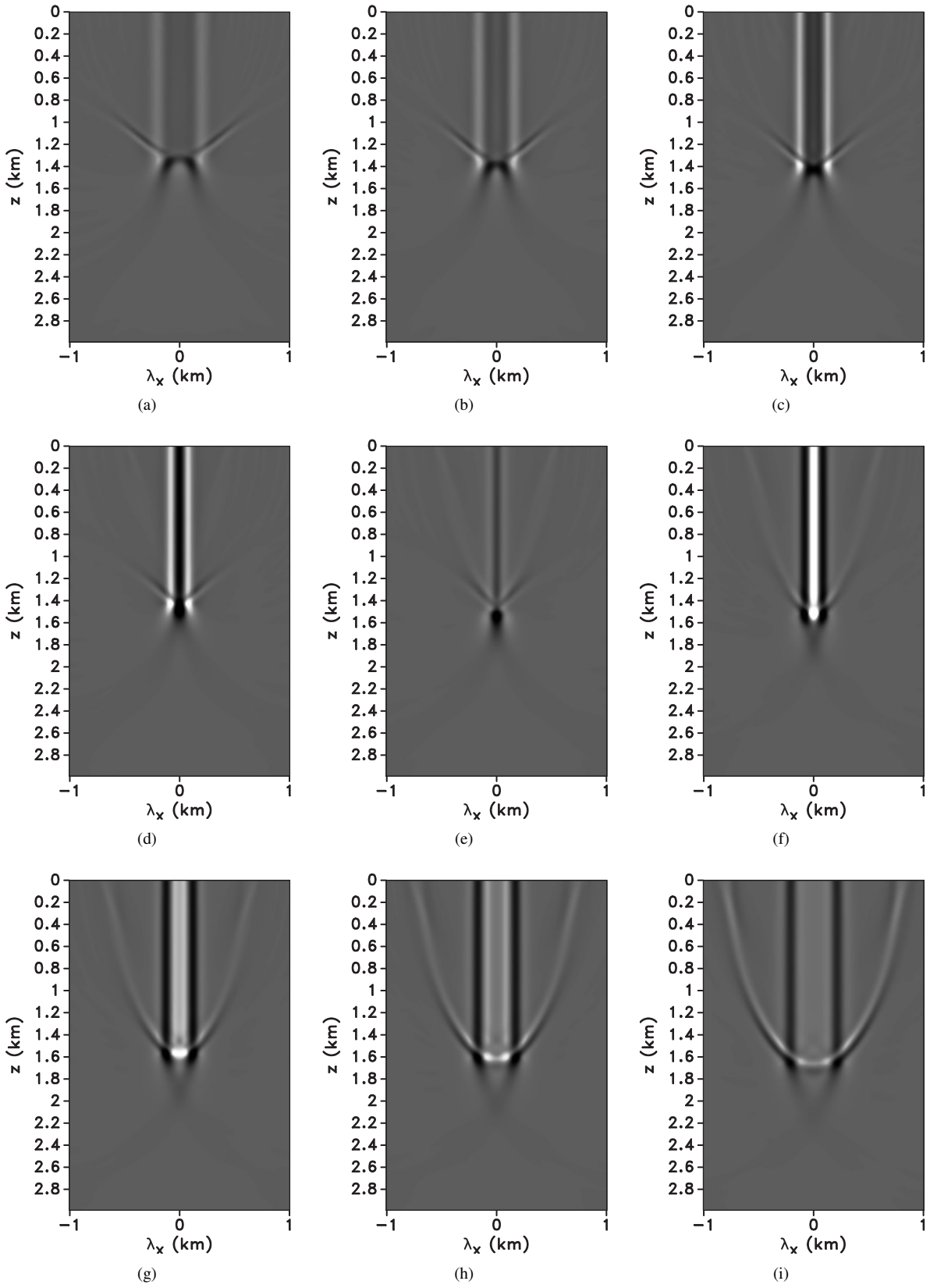


Figure 8. Model error sensitivity with space-lag gathers: (a) -12%, (b) -9%, (c) -6%, (d) -3%, (e) 0%, (f) +3%, +(g) +6%, (h) +9% and (i) +12% velocity perturbation in the top layer. Note that the maximum of backscattered energy happens with the correct velocity shown in panel (e).

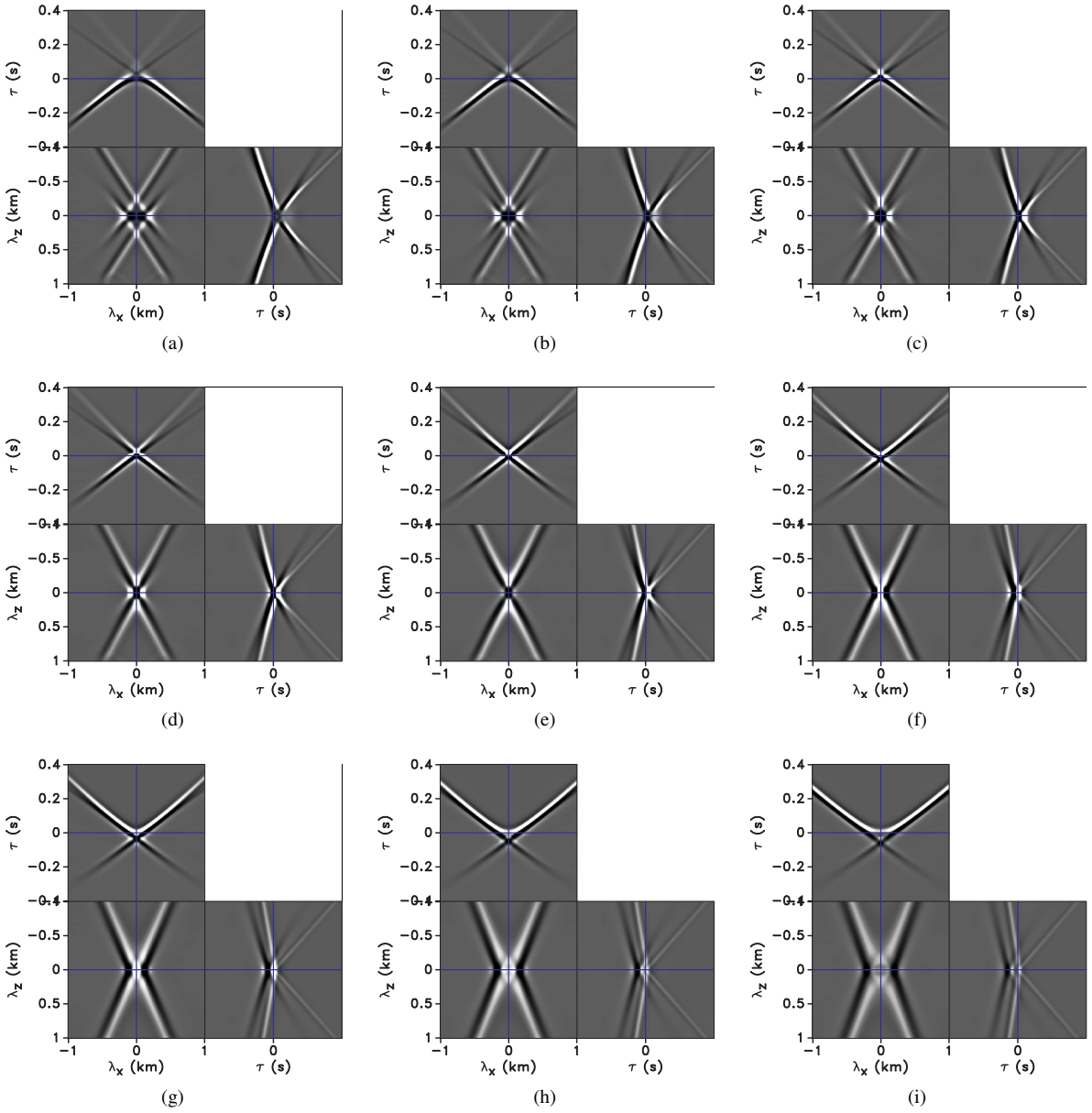


Figure 9. Model error sensitivity with CIP gathers: (a) -12%, (b) -9%, (c) -6%, (d) -3%, (e) +0%, (f) +3%, (g) +6%, (h) +9% and (i) +12% velocity perturbation in the top layer.

Here $P(\tau) = |\tau|$ and $P(\lambda_x) = |\lambda_x|$ are functions that penalize the backscattered energy away from zero lags, thus defining the residual that we need to minimize trough inversion.

For common image points we can use the objective function

$$J_{\mathbf{c}} = \frac{1}{2}\|P(\boldsymbol{\lambda},\tau)\left[R^{tr}(\boldsymbol{\lambda},\tau) + R^{rt}(\boldsymbol{\lambda},\tau)\right]\|_2^2. \qquad (9)$$

Here, $P(\boldsymbol{\lambda},\tau)$ is the penalty function for CIPs.

The penalty function is designed to measure the deviation or error between actual extended images and our notion for correct extended images. For CIGs we have a definite criterion, we know that the backscattered energy has to map to zero lag, that is why we can use the absolute value as penalty function. However, for CIPs the penalty operator is more complex. We use the correct CIP as reference for constructing the penalty function $P(\boldsymbol{\lambda},\tau)$ similar to the one proposed by (Yang et al., 2012). The correct CIP, shown in Figure 9(e) has the right focusing within the acquisition limitations. More generally, we could use a demigration/migration process to assess correct focusing at a given CIP position, and to infer the shape of the penalty operator.

Figures 10(a) to 10(c) show the penalty functions for

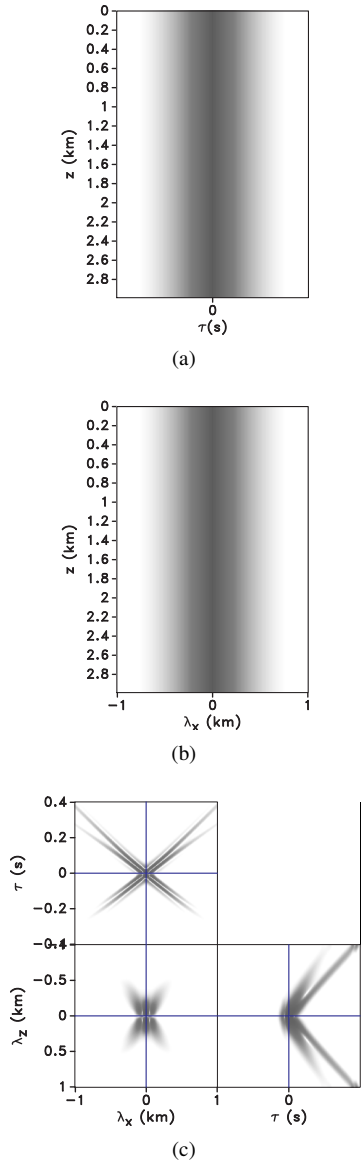


Figure 10. Penalty functions for time-lag gathers (a), space-lag gathers (b) and CIP gathers. Grey and white colors represent low and high penalty, respectively.

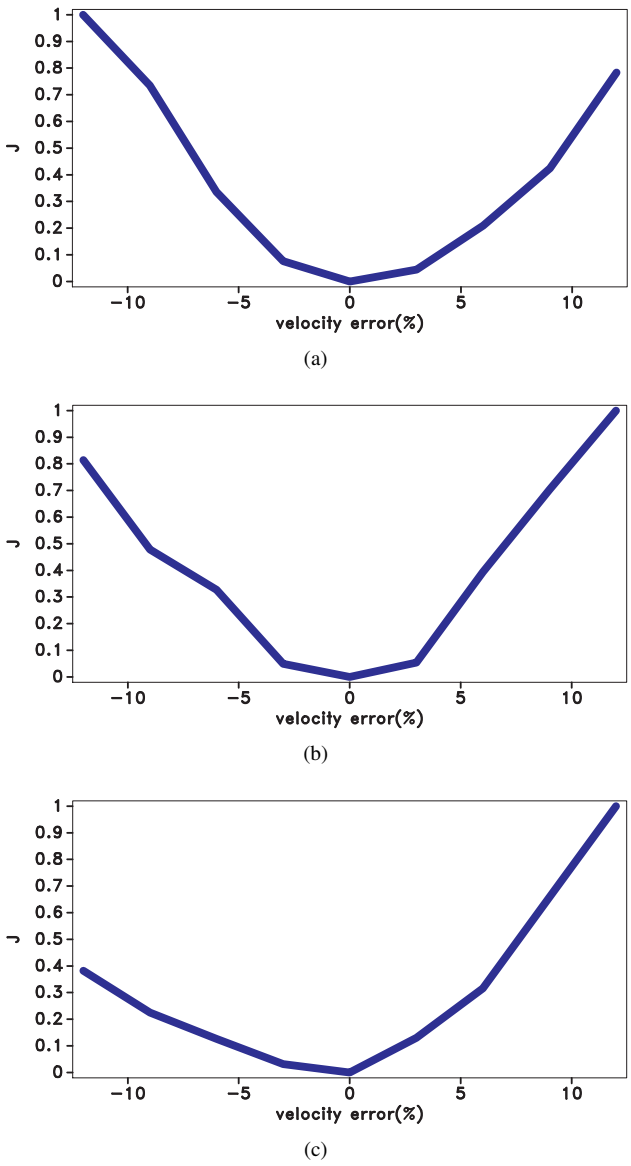


Figure 11. Normalized objective functions for time-lag gathers J_τ (a), space-lag gathers J_{λ_x} (b) and CIP gathers $J_{\mathbf{c}}$.

time-lag, space-lag and CIP gathers respectively. The objective functions for our synthetic example are shown in Figures 11(a) to 11(c) for time-lag gathers, space-lag gathers and common image point gathers respectively. One can see that in all three cases the OF minimizes at the correct model. If we want to optimize the model such as we maximize the backscattered events we need to consider two variables: the velocity model and the interface geometry. In our example the sharp interface depends linearly with the velocity model.

4 EXAMPLES

In this section we illustrate the backscattered events visible on extended images constructed based on a modified Sigsbee 2A model (Paffenholz et al., 2002). We modify the model by salt flooding (extending the salt to the bottom of the model) to avoid backscattering from the base of salt, therefore we focus on the reflections from the top of salt only. For this example we fix the receiver array on the surface, and we use 100 shots evenly sampled on the surface to build the image. For the migration model we use the stratigraphic velocity which shows sharp interfaces in the sediment section, in addition the interface corresponding with the top of salt. Figure 12(d) shows the

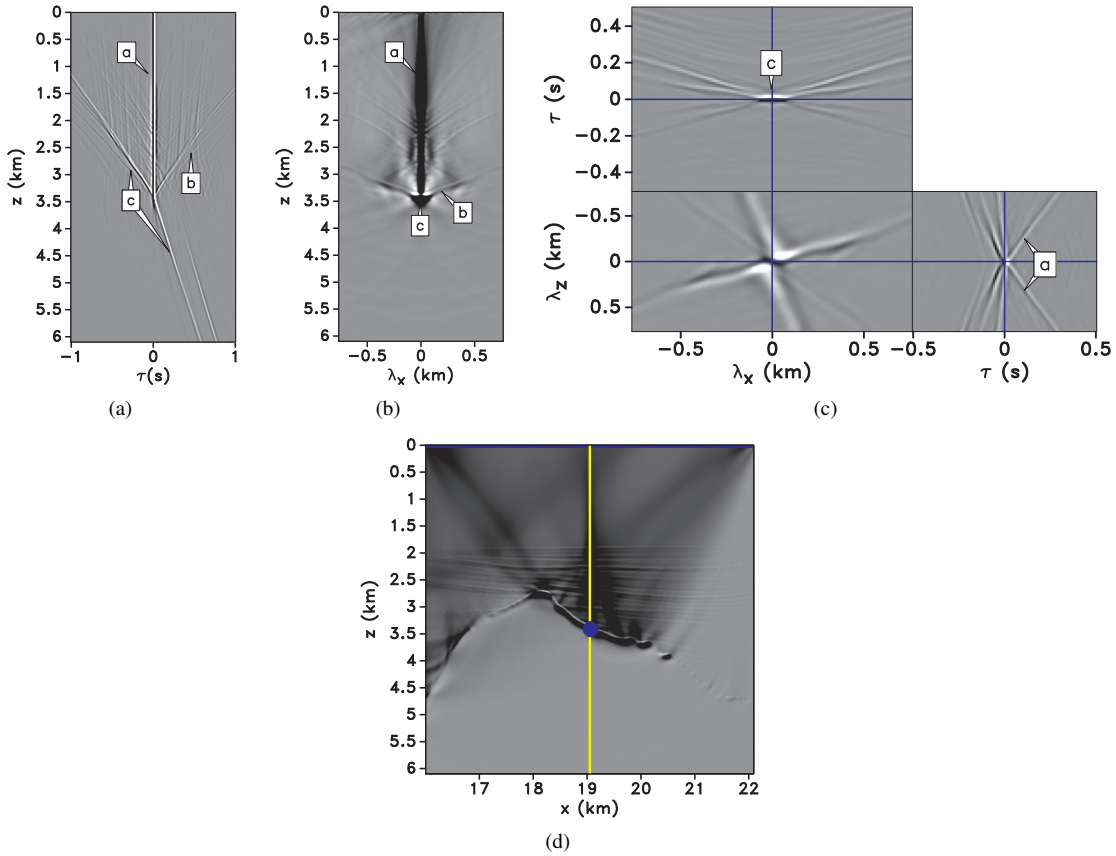


Figure 12. Sigsbee analysis: time-shift gather (a), space-lag gather (b), common image point (c) and RTM image (d). The vertical line and thick point shown in the RTM image shows the CIG and CIP locations respectively.

conventional image for our modified Sigsbee model, note the strong backscattered energy above the salt.

Figure 12(a) shows a time-lag gather calculated at x=19.05km. We can see that the gather is very complex, but we can easily identify the backscattered energy indicated with letter "a" in Figure 12(a). In this case, the backscattered energy maps directly to $\tau = 0$ because we use the correct velocity model. We can also identify the events corresponding to the cross-correlation between reflected waves from the source and receiver side $R^{rr}(z, \tau)$, indicated with letter "b". The $R^{rr}(z, \tau)$ events have positive slope (given by the sediment velocity at the interface) and are visible for $\tau > 0$. We can also observe a abrupt change in the slope of the primary reflection corresponding the sediment-salt interfaces at the top of salt indicated with letter "c".

Figure 12(b) shows a space-lag common image gather extracted at the same location. The backscattered energy maps toward $\lambda_x = 0$, indicated with letter "a". We see again the $R^{rr}(z, \lambda_x)$ case, indicated with letter "b", where the energy is mapped away from zero lag. Even though we are using the correct model, we still see energy away from $\lambda_x = 0$. This indicates that additional processing is needed before we can use space-lag gathers for model update with wave equation tomography.

Figure 12(c) shows a common image point extracted at the top of salt interface at $(x, z) = (19.05, 3.4)km$. Despite the complexity of this image, we can still identify similar patterns as shown in Figure 9(e). The backscattered events are mapped to $\tau > 0$ in the $\tau - \lambda_z$ plane, indicated with letter "a". In this plane we can separate with the individual contributions from $R^{tr}(\mathbf{x}, \boldsymbol{\lambda}, \tau)$ (which maps to $\lambda_z < 0$ and $\tau > 0$), and $R^{rt}(\mathbf{x}, \boldsymbol{\lambda}, \tau)$ (which maps to $\lambda_z > 0$ and $\tau > 0$), because they are imaged into two different events, whereas in the common image gathers discussed before we cannot differentiate the individual contributions, because both cases map to zero lag. The image of the reflector maps as a point to zero lag in the $\tau - \lambda_x$ plane (indicated with letter "c").

Understanding the backscattered energy in the extended images for complex scenarios is the first step in using these events for migration velocity analysis. In this report, we used wavefield decomposition to analyze the patterns of the backscattered energy in conventional and extended images. Although effective, wavefield decomposition can be very costly, specially for 3D models. In practice we need to use filtering of the extended images to isolate the events corresponding to the backscattered energy. How we can effectively implement this operation remains subject to future research.

5 CONCLUSIONS

RTM backscattered events maps to zero lag in the extended images when the velocity is correct. This means that the reflected receiver wavefield travels in perfect synchronization with the source wavefield and vice versa. We demonstrate that the RTM backscattered energy is sensitive to kinematics errors in the velocity model. The backscattered energy in the final image should not be considered as an artifact or a drawback of the imaging method; rather, the backscattered energy should be maximized in the image in order to ensure an optimum velocity model. The analysis of backscattered energy on extended images provide a definite criterion to update velocity models with salt interfaces (i.e in the Gulf of Mexico). Further tests are needed to develop automated velocity model update based on the maximization of the RTM backscattered energy. Our analysis also shows that some energy is mapped away from zero space-lag when we use RTM. This observation suggest that backscattered events should be taken into account in the design of objective functions in wavefield tomography using primary reflections information.

6 ACKNOWLEDGMENTS

Esteban Díaz would like to thank to Mariana Carvalho and Tongning Yang for insightful discussions with the common image point gathers analysis. The reproducible numeric examples in this paper use the Madagascar open-source software package freely available from http://www.reproducibility.org. This research was supported in part by the Golden Energy Computing Organization at the Colorado School of Mines using resources acquired with financial assistance from the National Science Foundation and the National Renewable Energy Laboratory.

REFERENCES

Baysal, E., D. D. Kosloff, and J. W. C. Sherwood, 1983, Reverse time migration: Geophysics, **48**, 1514–1524.

———, 1984, A two-way nonreflecting wave equation: Geophysics, **49**, 132–141.

Claerbout, J. F., 1985, Imaging the earth's interior: Blackwell Scientific Publications, Inc.

Fei, T. W., Y. Luo, and G. T. Schuster, 2010, De-blending reverse-time migration: SEG Technical Program Expanded Abstracts, **29**, 3130–3134.

Fletcher, R. F., P. Fowler, P. Kitchenside, and U. Albertin, 2005, Suppressing artifacts in prestack reverse time migration: SEG Technical Program Expanded Abstracts, **24**, 2049–2051.

Gazdag, J., 1978, Wave equation migration with the phase-shift method: Geophysics, **43**, 1342–1351.

Gazdag, J., and P. Sguazzero, 1984, Migration of seismic data by phase shift plus interpolation: Geophysics, **49**, 124–131.

Guitton, A., B. Kaelin, and B. Biondi, 2007, Least-squares attenuation of reverse-time-migration artifacts: Geophysics, **72**, S19–S23.

Kaelin, B., and C. Carvajal, 2011, Eliminating imaging artifacts in rtm using pre-stack gathers: SEG Technical Program Expanded Abstracts, **30**, 3125–3129.

Liu, F., G. Zhang, S. A. Morton, and J. P. Leveille, 2011, An effective imaging condition for reverse-time migration using wavefield decomposition: Geophysics, **76**, S29–S39.

McMechan, G. A., 1983, Migration by extrapolation of time-dependent boundary values: Geophysical Prospecting, **31**, 413–420.

Paffenholz, J., B. McLain, J. Zaske, and P. Keliher, 2002, Subsalt multiple attenuation and imaging: Observations from the sigsbee 2b synthetic dataset: 72nd Annual International Meeting, SEG, Expanded Abstracts, 2122–2125.

Rickett, J. E., and P. C. Sava, 2002, Offset and angle-domain common image-point gathers for shot-profile migration: Geophysics, **67**, 883–889.

Sava, P., and S. Fomel, 2006, Time-shift imaging condition in seismic migration: Geophysics, **71**, S209–S217.

Sava, P., and I. Vasconcelos, 2011, Extended imaging conditions for wave-equation migration: Geophysical Prospecting, **59**, 35–55.

Sava, P., and I. Vlad, 2011, Wide-azimuth angle gathers for wave-equation migration: Geophysics, **76**, S131–S141.

Sava, P. C., and S. Fomel, 2003, Angle-domain common-image gathers by wavefield continuation methods: Geophysics, **68**, 1065–1074.

Shen, P., W. W. Symes, and C. C. Stolk, 2003, Differential semblance velocity analysis by wave-equation migration: SEG Technical Program Expanded Abstracts, **22**, 2132–2135.

Whitmore, N. D., 1983, Iterative depth migration by backward time propagation: SEG Technical Program Expanded Abstracts, **2**, 382–385.

Yang, T., and P. Sava, 2010, Moveout analysis of wave-equation extended images: Geophysics, **75**, S151–S161.

Yang, T., J. Shragge, and P. C. Sava, 2012, Illumination compensation for image-domain wavefield tomography: CWP, **712**, 93–110.

Youn, O. K., and H. Zhou, 2001, Depth imaging with multiples: Geophysics, **66**, 246–255.